Research Article Vol. 30, No. 6 / 14 Mar 2022 / Optics Express 8991
Optics EXPRESS

# Large-aperture single-mode 795 nm VCSEL for chip-scale nuclear magnetic resonance gyroscope with an output power of 4.1 mW at 80 ℃

YINLI ZHOU,[1] YUCHEN JIA,[2] XING ZHANG,[1,3] JIANWEI ZHANG,[1] ZHANCHAO LIU,[2,4] YONGQIANG NING,[1] AND LIJUN WANG[1]

[1]*State Key Laboratory of Luminescence and Applications, Changchun Institute of Optics, Fine Mechanics and Physics, Chinese Academy of Sciences, Changchun, China*
[2]*Beihang University, Beijing 100191, China*
[3]*zhangx@ciomp.ac.cn*
[4]*liuzhanchao@hotmail.com*

**Abstract:** Transverse optical confinement in oxide-confined vertical-cavity surface-emitting lasers (VCSELs) crucially depends on thickness of oxide layer and its position relative to a standing wave. Modifying the structure reduces the overlap between the oxide layer and the standing wave as well as effective refractive index difference between core and cladding of the VCSEL that subsequently decreases of the number of transverse modes and increases the mode extension beyond oxide aperture. A 795 nm VCSEL is designed and fabricated with this concept. The proposed device achieves high single-mode operation of 4.1 mW at 80 °C, SMSR of 41.68 dB, and OPSR of 27.4 dB. VCSEL is applied in a nuclear magnetic resonance gyroscope (NMRG) system as pump source due to its excellent device performance and satisfactory test results are obtained.



## 1. Introduction

Vertical-cavity surface-emitting lasers (VCSELs) present many attractive properties, such as surface emission, circular and low divergent output beam, and integration into two-dimensional arrays [1,2]. Single-transverse mode VCSELs (SM-VCSELs) are preferred optical sources for small low-power atomic sensors, including chip-scale atomic clocks, magnetometers, and gyroscopes [3–5]. VCSEL is required to work at high temperatures with single-mode and low-power consumption and its output power determines the polarizability of alkali metal atoms and ultimately affects signal-to-noise ratio of the gyro in the application of NMRG [6].

Oxide aperture diameter must be sufficiently small (< 4 μm) in a conventional oxide-confined SM-VCSEL to support the fundamental mode alone. However, high series resistance (typically > 200 Ω for GaAs-based VCSEL) from the small aperture limits output power and reliability due to excessive current-induced self-heating and high current density. Although a large aperture reduces the electrical resistance, delays thermal rollover, and enables high output power, it can also lead to multimode operation. Single-mode operation can be achieved by introducing mode-selective gain or loss in an otherwise multimode VCSEL to force it to oscillate in the low-order fundamental transverse mode alone. Various alternative approaches, including photonic crystal [7,8] or holey-structure integrated [9], Zn-diffusion [10,11] and surface relief [12–14] VCSELs, have been investigated. These methods require additional process steps and very high process accuracy compared with conventional oxide-confined SM-VCSEL.

It is a very attractive idea to achieve high power operation of an intrinsic SM-VCSEL based on a large oxide aperture by means of epitaxial structure design without introducing additional process steps. One of the design concepts is to optimize the epitaxial structure of the VCSEL

#450118 https://doi.org/10.1364/OE.450118
Journal © 2022 Received 30 Nov 2021; revised 12 Feb 2022; accepted 13 Feb 2022; published 3 Mar 2022

Optics EXPRESS

with double oxide layers to make the high-order transverse modes have high lateral leakage loss, thus promoting the single–mode lasing in the fundamental transverse mode. The oxide aperture of the VCSEL supporting single-mode operation can be increased to ~5 μm [15,16]. Another design concept of single-mode VCSEL based on large oxide aperture has been reported by several research teams [17–21]. In our paper we applied a design proposed in Ref.21. The reduced number of confined modes in the oxide aperture and the proper spreading of optical field beyond the aperture when the aperture is moved away from the active layer introduce large loss of high-order modes and thus allow the VCSEL to maintain a stable fundamental transverse-mode operation. We demonstrated the experimental results of a 6 μm large-aperture SM-VCSEL according to this design concept. A maximum single-mode output power of 4.1 mW with side-mode suppression ratio (SMSR) of 41.68 dB was achieved at a temperature of 80 °C. To the best of our knowledge, this performance for single-mode VCSELs operating at high temperatures is optimal and can meet the needs of atomic gyroscope applications. First, the basic epitaxy structure of VCSELs is designed. The device is then fabricated and the photoelectric performance is tested. Finally, the VCSEL is integrated into a miniaturized NMRG prototype, and the atomic polarizability and magnetometer sensitivity are measured.

## 2. Device design and fabrication

A schematic of the epitaxial and device structure is shown in Fig. 1. The active region is composed of three 6.8 nm compressively strained $In_{0.125}Al_{0.14}Ga_{0.735}As/Al_{0.3}Ga_{0.7}As$ quantum wells. Top/bottom DBRs consist of 24/38 pairs of $Al_{0.12}Ga_{0.88}As/Al_{0.9}Ga_{0.1}As$ layers separated by 20 nm thick grading layers. The oxide layer is realized with a 20 nm thick $Al_{0.98}Ga_{0.02}As$ layer inserted between the active region and the p-DBR. A part of $Al_{0.98}Ga_{0.02}As$ is transformed into amorphous $(Al_xGa_{1-x})_2O_3$ to form oxide aperture after wet oxidation. The edges of the device are along the [1 1 0] and [$\bar{1}$ 1 0] crystallographic axis respectively.

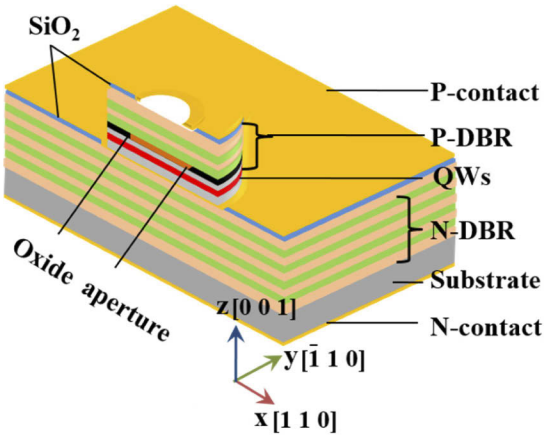


**Fig. 1.** Schematic of VCSELs

Lasing wavelength of VCSELs is determined by resonance wavelength ($\lambda_c$) in the cavity. Effective gain at λc is called cavity-mode gain. The VCSEL operates at temperatures over 80 °C when used as a pump source for the NMRG. Gain spectra of 6.8 nm $In_{0.125}Al_{0.14}Ga_{0.735}As/Al_{0.3}Ga_{0.7}As$ quantum wells at different temperatures were calculated to maximize the cavity-mode gain of VCSEL at this temperature. Carrier density for the gain spectrum calculation was set to $5\times10^{18}$ $cm^{-3}$. As shown in Fig. 2(a), the cavity mode gain at different temperatures was indicated by the solid red box. Figure 2(b) shows the variation of the resonant wavelength and the cavity mode gain with temperature. VCSEL presents the maximum cavity-mode gain when the temperature

Optics EXPRESS

range is 80 °C–90 °C and corresponds to gain-cavity detuning of ~10.8 nm at room temperature. $\lambda_c$ is 794.44 nm at 80 °C.

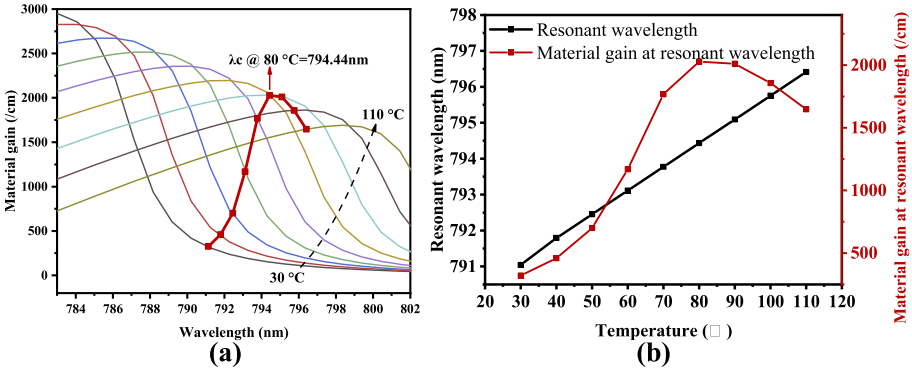


**Fig. 2.** (a) Gain spectra of 6.8 nm $In_{0.125}Al_{0.14}Ga_{0.735}As/Al_{0.3}Ga_{0.7}As$ quantum wells at different temperatures. (b) Variation of the resonant wavelength and the cavity mode gain with temperature

The transverse optical confinement in oxide-confined VCSEL is achieved by partially oxidizing the AlGaAs layer with high Al component (98%) and reducing its refractive index to form a cylindrical waveguide with refractive index difference $\Delta_{neff}$. $\Delta_{neff}$ is the refractive index difference between unoxidized core and oxidized cladding in VCSEL. The effective refractive index of the core ($N_{core}$) and cladding ($N_{clad}$) is calculated as follows:

$$N_{clad} = \frac{\int n_{clad} * E_z * dz}{\int E_z * dz}, \qquad N_{core} = \frac{\int n_{core} * E_z * dz}{\int E_z * dz}, \tag{1}$$

where $n_{core}$ and $n_{clad}$ are the material refractive index and $E_z$ is the standing wave distribution of the electric field along the Z direction. Decreasing the overlap between the oxide aperture and the standing wave distribution can reduce $\Delta_{neff}$ and thus minimize diffraction and optical confinement at the the aperture. $E_z$ and refractive index along the Z direction in the core region of the VCSEL with traditional and improved structure are illustrated in Fig. 3. As shown in Fig. 3(a), the 30 nm oxide layer is located at the first standing wave node adjacent to the active cavity while $\Delta_{neff}$ in this configuration is ~0.006 in the conventional VCSEL. A new design is adopted in this study to move the oxide layer to the third standing wave node far from the active cavity, reduce its thickness to 20 nm, and obtain a $\Delta_{neff}$ of ~0.002.

The analysis theory of the transverse optical modes in VCSEL has experienced continuous development and improvement. As early as 1995, G. R. Hadley proposed that the effective refractive index of VCSEL varies along the radial direction, and the effective refractive index of different regions is directly related to the resonance wavelength of the region [22]. This effective refractive index model provides a correct development direction for the design of oxide-confined VCSEL. Based on the vector solution of Maxwell's equations, an all-optical laser model which can deal with diffraction effect is reported [23]. This model can directly calculate the threshold materials gain of VCSEL. It is found that when the oxide layer more overlaps with the standing wave distribution in the VCSEL cavity, the threshold gain of the device decreased, but the restriction of the oxide aperture on the higher-order mode increased, which reduced the mode selection characteristic. When the oxide layer less overlaps with the standing wave, the mode limitation is weakened, and the threshold gain of the device increases. However, the mode selection characteristic of the device increases with the higher diffraction loss of the higher-order mode. At present, the theory of calculating the internal optical mode of VCSEL by Maxwell's equations and the boundary conditions of the core-cladding interface has reached

Optics EXPRESS

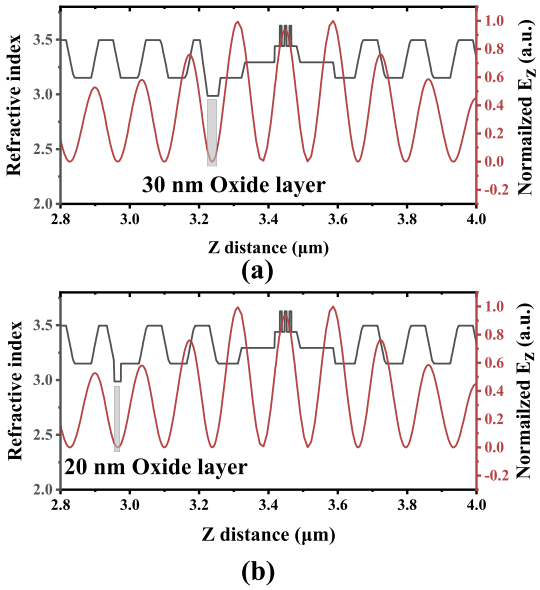


**Fig. 3.** Normalized Ez and refractive index along the Z direction in the core region of the VCSEL with (a) traditional and (b) improved structures

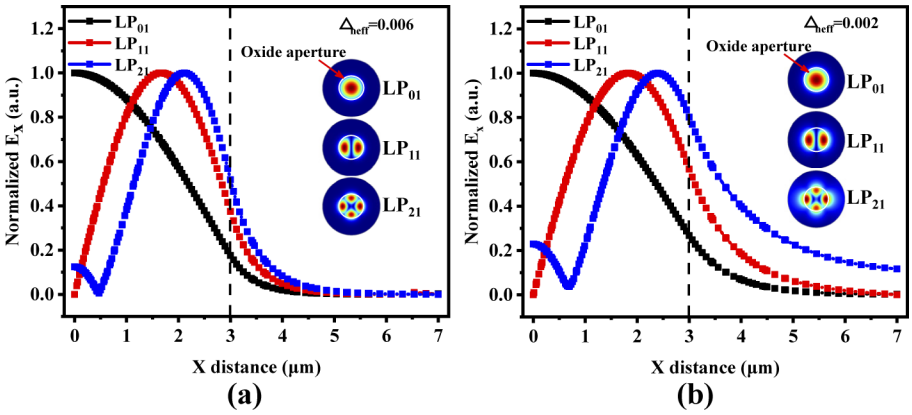


**Fig. 4.** Distribution of $LP_{01}$, $LP_{11}$, and $LP_{21}$ modes along the radial direction of VCSELs with (a) $\Delta_{neff} = 0.006$ and (b) $\Delta_{neff} = 0.002$

a certain degree of maturity. The tranverse modes in VCSEL can be characterized in terms of $LP_{mn}$ modes [24], where m is the azimuthal mode number and n is the radial mode number. Based on this method, we calculated the transverse mode distributions in VCSELs with different $\Delta_{neff}$. The oxide aperture diameter is set to 6 μm. A maximum of 12 transverse modes exists when $\Delta_{neff}$ is equal to 0.006, and the number decreases to 3 as $\Delta_{neff}$ decreases to 0.002. The 1- and 2-D distributions of the first three transverse modes $LP_{01}$, $LP_{11}$, and $LP_{21}$ along the radial direction (X direction) of the above two VCSEL designs are shown in Fig. 4. The edge of the oxide aperture in the X direction is marked with a dashed black line. As shown in Fig. 4(a), the aperture presents strong optical confinement when $\Delta_{neff}$ is 0.006 and only a small part of light leaks out of the aperture under all three transverse modes. The optical confinement weakens and the light leakage increases when $\Delta_{neff}$ is 0.002. Compared with the fundamental transverse mode

Optics EXPRESS

$LP_{01}$, more light of the two higher-order modes leaks out of the aperture. The oxidized region is electrically insulated, confines carriers to the aperture of the VCSEL, and results in large optical loss outside the aperture. Therefore, the VCSEL with the new configuration can introduce large high-order mode loss to prevent it from reaching the lasing threshold and ensure that the VCSEL with large oxide aperture is operational in the fundamental transverse mode.

The device is fabricated using a standard process. A 20 μm mesa is formed with inductively coupled plasma reactive ion etching. A 6 μm oxide aperture is formed by selectively oxidizing the $Al_{0.98}Ga_{0.02}As$ layer. The 300 nm $SiO_2$ insulation layer covers the upper surface of the entire device. The electrical injection window is formed by etching the $SiO_2$ layer in the center of the mesa. The metal layer was deposited with a magnetron sputtering equipment, and a 10 μm light-emitting aperture is formed using a lift-off process step.

## 3. Experimental results and discussions

The VCSEL chip for testing was packaged in a TO56 form and installed on a commercial laser diode mount for temperature and current control. The current and temperature control accuracy are 0.001 mA and 0.01 °C, respectively. Spectrum-current characteristic of the VCSEL at different tempertures is shown in Fig. 5(a). The device can maintain stable single-mode operation when the current is below 5 mA. The lasing wavelength is 794.45 nm at 80 °C and 5 mA and consistent with the designed $\lambda_c$. Meanwhile, the SMSR is 41.68 dB. The separation between the fundamental and the first excited mode is increase form 0.5 nm to 0.82 nm with current increasing from 3 mA to 5 mA at 80°C. This is because under high current density, the heat generation of the device increases and the temperature of the core is higher than that of the clad, resulting in an increase in the $\Delta_{neff}$ compared with the case of cold cavity. The heating-induced refractive index change, increases the number of effectively confined modes and can limit the maximum aperture diameter for SM operation [25]. Figure 5(b) shows the change of SMSR with current at different temperatures. The majority of SMSR values are larger than 40 dB, and the maximum SMSR value is 51.6 dB at a current of 4.2 mA and a temperature of 40 °C. Fig. 5(c) shows a linear relationship between the central wavelength and the square value of the current. This is because the main heat generation mechanism in VCSEL is joule effect, and joule heat has a linear relationship with the square value of current. The emission wavelength of VCSEL is linearly related to the temperature of the device.

The power–current-voltage characteristic of the VCSEL at different tempertures is presented in Fig. 6(a). The maximum output power drops from 4.85 mW to 4.1 mW as the temperature increased from 25 °C to 80 °C. The resistance of the device calculated according to the I-V curve is ~50 Ω and hardly changes with temperature, which is far less than the resistance (~200 Ω) of the GaAs-based VCSEL with small oxide diameter (~3 μm). As shown in Fig. 6(b), the slope efficiency of the device drops slightly from 1.13 W/A to 1.02 W/A.The threshold current of the device is a function of temperature and higher than that of the conventional oxide-confined SM-VCSEL (typically < 0.5 mA) due to the large oxidation aperture and the introduction of partial fundamental mode optical losses in the new design. Different from that of the expected design conclusion, the threshold current of the device reaches a minimum of 0.89 mA at 40 °C and increases to 1 mA at 80 °C. As shown in Fig. 2, VCSEL exhibits the maximum cavity-mode gain when the temperature range is 80 °C–90 °C. This phenomenon is caused by the decrease of internal quantum efficiency of VCSEL due to the degradation of carrier confinement within QWs at high temperatures.

The 2-D distribution of near fields of VCSEL with different current and temperature is shown in Fig. 7(a). All near fields present a single-lobe Gaussian-like distribution that indicates the working state of the single transverse mode of the VCSEL. The far field patterns of the device at a distance of 30 mm in the p-polarization direction under different current and temperature is shown in Fig. 7(b). D4-Σ ISO method was used to calculate the beam width, and the far-field

Optics EXPRESS

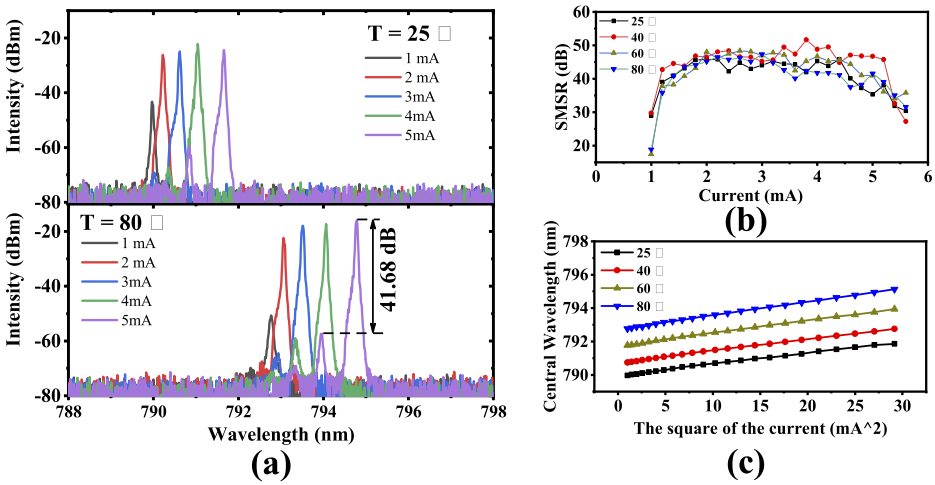


**Fig. 5.** Spectral characteristics with (a) current under 25 °C and 80 °C of VCSELs. (b) Variation of the SMSR with current under different temperature. (c) Variation of the central wavelength with the square of current under different temperature

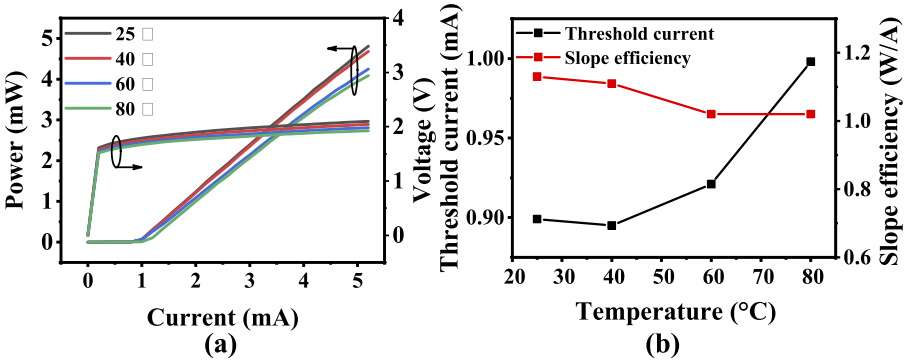


**Fig. 6.** (a) Power–current-voltage characteristics of the device. (b)variation of threshold current and slope efficiency with temperature.

divergence angle of the device was calculated according to the far-field wide Angle method. At 80 °C and 5 mA, the calculated divergence angle of the far field in the p-polarization direction of the device is 16.4°. The power of the s-polarization direction is too low to measure the far field.

The polarization characteristic of VCSEL is verymportant in the application of atomic sensing applications [26,27]. The output power of the VCSEL along different polarization angles at 80 °C and 5 mA is depicted in Fig. 8(a). Due to the electro-optic effect, VCSEL has a preferred direction of polarization along [1 1 0] or [$\bar{1}$ 1 0] crystallographic axis [28,29]. The two orthogonal polarization directions of maximum and minimum power can be defined as p- and s-polarization, respectively. By comparing the direction of the polarizer with that of the chip edge, the p-polarization direction at 80 °C and 5 mA is along the crystallographic axis of [1 1 0]. . The outline of the power-angle curve is like the symbol "∞". Orthogonal polarization suppression ratio (OPSR) is calculated at 24.07 dB. The optical power in directions other than p- and s-polarization modes represent different components of the major p-polarization according to Malus's law. The polarization-resolved spectrum at 80 °C and 5 mA is shown in Fig. 8(b). The optical spectrum without polarizer clearly shows the existence of three transverse modes

Optics EXPRESS

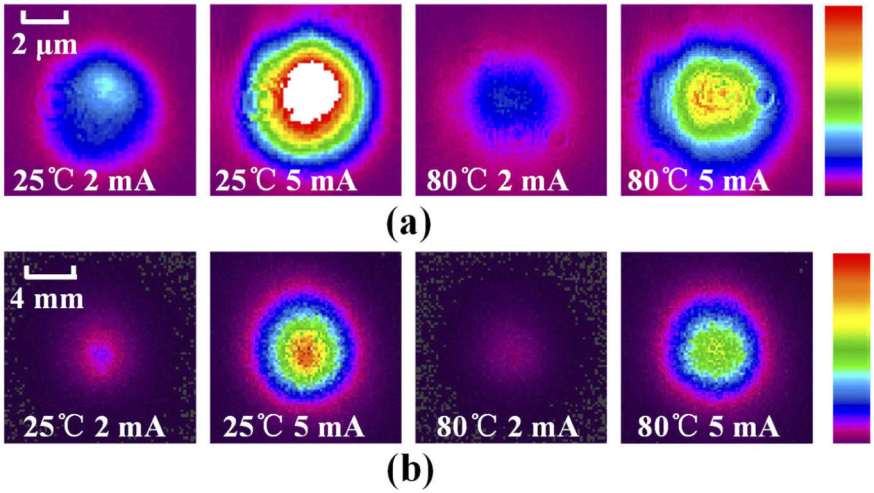


**Fig. 7.** (a) Near field patterns of the device at different current and temperature. (b) Far field patterns of the device in the p-polarization direction at different current and temperature

$LP_{01}$, $LP_{11}$, and $LP_{21}$ in the VCSEL under high injection current. Excitation of high-order modes $LP_{11}$ and $LP_{21}$ is impossible due to high losses. Only the fundamental transverse mode $LP_{01}$ can be seen in the spectrum at the p-polarization without any high-order modes, thereby indicating that high-order modes present different polarization directions from the fundamental mode. The maximum peak-to-peak difference between p- and s-polarization modes is 27.46 dB. This high OPSR benefits from the use of the newly designed VCSEL with excellent monochromaticity and high output power. Unfortunately, since not any polarization selection method was adpoted, the principal polarization direction of the device varies randomly between the two axes as the operating current and temperature change. In the follow-up work, polarization selective grating structures will be introduced to stabilize the polarization.

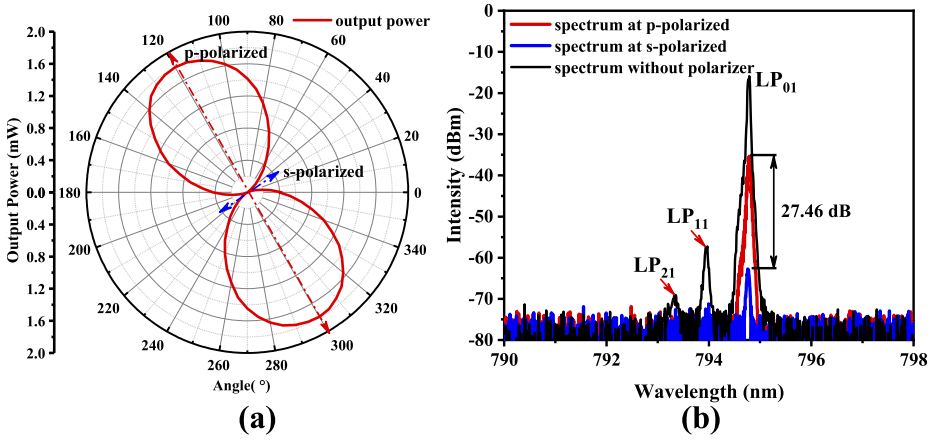


**Fig. 8.** (a) Optical power of VCSEL in different polarization angles at 80 °C. (b) Polarization-resolved spectrum of VCSEL at 80 °C and 5 mA.

The device was integrated into the miniaturized NMRG prototype to explore the performance of VCSEL further and test the atomic polarizability and magnetometer sensitivity. As shown in Fig. 9, the experimental setup is composed of a pump laser, probe laser, optical components,

Optics EXPRESS

vapor cell, oven, photodiode detector, and coils. The glass vapor cell contains alkali metal atom Rb and Xe gas, with $N_2$ as the quenching gas and $^4$He as the buffer gas. A four-layer cylindrical magnetic shield is used to reduce the external magnetic field. The working principle of NMRG can be referred to in [30].

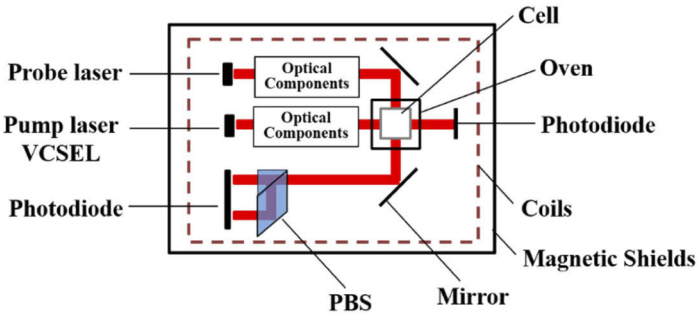


**Fig. 9.** Diagram of the NMRG prototype.

The atomic spin polarizability directly affects the signal-to-noise ratio of NMRG and is very important to the gyro performance. The polarization is mainly determined by the pumping light source to ensure that it can reflect the performance of the light source. The sensitivity of magnetometer is an important performance index that can reflect noise characteristics of NMRG and directly related to noise characteristics of the light source. Using VCSEL as pump source, the measured atomic spin polarization and sensitivity of NMGR system is 5.52% and 3.2 Pt/Hz$^{1/2}$, respectively. These results revealed that the excellent performance of the VCSEL can meet the initial application of NMRG.

## 4. Conclusion

We proposed a 795 nm SM-VCSEL with large oxide aperture. SM operation of large apertures can be achieved by refining the high aluminum oxide layer and appropriately transferring it to the mode node away from the active cavity. This design requires modification of only a few p-DBR pairs. The result maintains high-power single-transverse mode operation of the device due to a significant reduction in the number of transverse modes in the VCSEL and the introduction of high mode loss. The maximum output power is 4.1 mW and the SMSR is 41.68 dB at 80 °C. Excellent monochromaticity also results in a high OPSR value of 27.4 dB. Application verification in the NMRG system further proves the high performance of VCSEL with the new design.

**Funding.** National Key Research and Development Program of China (2018YFB2002400); National Natural Science Foundation of China (11774343, 52172165, 61804151, 61874117, 61874119, 62104225); Jilin Scientific and Technological Development Program (20200401006GX).

**Disclosures.** The authors declare no conflicts of interest.

**Data availability.** Data underlying the results presented in this paper are not publicly available at this time but may be obtained from the authors upon reasonable request.

## References

1. A. Larsson, "Advances in VCSELs for communication and sensing," IEEE J. Sel. Top. Quant. Electron. **17**(6), 1552–1567 (2011).
2. A. Kasukawa, "VCSEL technology for green optical interconnects," IEEE Photonics J. **4**(2), 642–646 (2012).
3. J. Kitching, "Chip-scale atomic devices," Appl Phys. Rev. **5**(3), 031302 (2018).
4. S. Knappe, V. Gerginov, P. D. D. Schwindt, V. Shah, H. G. Robinson, L. Hollberg, and J. Kitching, "Atomic vapor cells for chip-scale atomic clocks with improved long-term frequency stability," Opt. Lett. **30**(18), 2351–2353 (2005).

Optics EXPRESS


5. J. W. Zhang, X. Zhang, H. B. Zhu, J. Zhang, Y. Q. Ning, L. Qin, and L. J. Wang, "High-temperature operating 894.6nm-VCSELs with extremely low threshold for Cs-based chip scale atomic clocks," Opt. Express **23**(11), 14763–14773 (2015).
6. N. A. Maleev, S. A. Blokhin, M. A. Bobrov, A. G. Kuz'menkov, M. M. Kulagina, and V. M. Ustinov, "Laser Source for a Compact Nuclear Magnetic Resonance Gyroscope," Gyroscopy Navig. **9**(3), 177–182 (2018).
7. T. Czyszanowski, M. Dems, and K. Panajotov, "Single mode condition and modes discrimination in photonic-crystal 1.3 mu m AlInGaAs/InP VCSEL," Opt. Express **15**(9), 5604–5609 (2007).
8. J.-H. Baek, D.-S. Song, I.-K. Hwang, H.-H. Lee, Y. Lee, Y.-G. Ju, T. Kondo, T. Miyamoto, and F. Koyama, "Transverse mode control by etch-depth tuning in 1120-nm GaInAs/GaAs photonic crystal vertical-cavity surface-emitting lasers," Opt. Express **12**(5), 859–867 (2004).
9. A. Furukawa, S. Sasaki, M. Hoshi, A. Matsuzono, K. Moritoh, and T. Baba, "High-power single-mode vertical-cavity surface-emitting lasers with triangular holey structure," Appl. Phys. Lett. **85**(22), 5161–5163 (2004).
10. J. W. Shi, Z. R. Wei, K. L. Chi, J. W. Jiang, J. M. Wun, I. C. Lu, J. Chen, and Y. J. Yang, "Single–mode, high–speed, and high–power vertical–cavity surface–emitting lasers at 850 nm for short to medium reach (2 km) optical interconnects," J. Lightwave Technol. **31**(24), 4037–4044 (2013).
11. J. W. Shi, Z. Khan, R. H. Horng, H. Y. Yeh, C. K. Huang, C. Y. Liu, J. C. Shi, Y. H. Chang, J. L. Yen, and J. K. Sheu, "High-power and single-mode VCSEL arrays with single-polarized outputs by using package-induced tensile strain," Opt. Lett. **45**(17), 4839–4842 (2020).
12. Å. Haglund, J. S. Gustavsson, J. Vukušić, P. Modh, and A. Larsson, "Single fundamental-mode output power exceeding 6 mW from VCSELs with a shallow surface relief," IEEE Photonics Technol. Lett. **16**(2), 368–370 (2004).
13. A. Al-Samaneh, M. Bou Sanayeh, M. J. Miah, W. Schwarz, D. Wahl, A. Kern, and R. Michalzik, "Polarization-stable vertical-cavity surface-emitting lasers with inverted grating relief for use in microscale atomic clocks," Appl. Phys. Lett. **101**(17), 171104 (2012).
14. J. Gustavsson, Å. Haglund, J. Vukušić, J. Bengtsson, P. Jedrasik, and A. Larsson, "Efficient and individually controllable mechanisms for mode and polarization selection in VCSELs, based on a common, localized, sub-wavelength surface grating," Opt. Express **13**(17), 6626–6634 (2005).
15. N. Ledentsov, V. A. Shchukin, N. N. Ledentsov, J.-R. Kropp, S. Burger, and F. Schmidt, "Direct evidence of the leaky emission in oxide–confined vertical cavity lasers," IEEE J. Quantum Electron. **52**(3), 1–7 (2016).
16. V. A. Shchukin, N. N. Ledentsov, J.-R. Kropp, G. Steinle, N. Ledentsov, S. Burger, and F. Schmidt, "Single–mode vertical cavity surface emitting laser via oxide–aperture–engineering of leakage of high–order transverse modes," IEEE J. Quantum Electron. **50**(12), 990–995 (2014).
17. R. Sarzala, T. Czyszanowski, M. Wasiak, M. Dems, L. Piskorski, W. Nakwaski, and K. Panajotov, "Numerical self-consistent analysis of VCSELs," Adv. Opt. Technol. **2012**, 1–17 (2012).
18. E. R. Hegblom, B. J. Thibeault, R. L. Naone, and L. A. Coldren, "Vertical cavity lasers with tapered oxide apertures for low scattering loss," Electron. Lett. **33**(10), 869–871 (1997).
19. K. D. Choquette, K. L. Lear, R. P. Schneider, and K. M. Geib, "Cavity characteristics of selectively oxidized vertical cavity lasers," Appl. Phys. Lett. **66**(25), 3413–3415 (1995).
20. Y. Liu, W. C. Ng, B. Klein, and K. Hess, "Effects of the spatial nonuniformity of optical transverse modes on the modulation response of vertical-cavity surface-emitting lasers," IEEE J. Quantum Electron. **39**(1), 99–108 (2003).
21. V. P. Kalosha, N. N. Ledentsov, and D. Bimberg, "Design considerations for large–aperture single–mode oxide–confined vertical–cavity surface–emitting lasers," Appl. Phys. Lett. **101**(7), 071117 (2012).
22. G. R. Hadley, "Effective index model for VCSELs," Opt. Lett. **20**(13), 1483–1485 (1995).
23. B. Demeulenaere, P. Bienstman, B. Dhoedt, and R. G. Baets, "Detailed study of AlAs-oxidized apertures in VCSEL cavities for optimized modal performance," IEEE J. Quantum Electron. **35**(3), 358–367 (1999).
24. R. Michalzik, *VCSELs: Fundamentals, Technology and Applications of Vertical-Cavity Surface-Emitting Lasers*, Vol. 166 of Springer Series in Optical Sciences (Springer-Verlag, 2013), Chap. 4.
25. N. N. Ledentsov, V. A. Shchukin, V. P. Kalosha, N. N. Ledentsov, J.-R. Kropp, M. Agustin, L. Chorchos, G. Stepinac, J. P. Turkiewicz, and J.-W. Shi, "Anti–waveguiding vertical–cavity surface–emitting laser at 850 nm: From concept to advances in high–speed data transmission," Opt. Express **26**(1), 445–453 (2018).
26. A. Al-Samaneh, M. Bou Sanayeh, S. Renz, D. Wahl, and R. Michalzik, "Polarization control and dynamic properties of VCSELs for MEMS atomic clock applications," IEEE Photon. Technol. Lett. **23**(15), 1049–1051 (2011).
27. F. Gruet, A. Al-Samaneh, E. Kroemer, L. Bimboes, D. Miletic, C. Affolderback, D. Wahl, R. Boudot, G. Mileti, and R. Michalzik, "Metrological characterization of custom-designed 894.6 nm VCSELs for miniature atomic clocks," Opt. Express **21**(5), 5781–5792 (2013).
28. M. P. van Exter, A.K. Jansen van Doorn, J. van Doorn, and J. P. Woerdman, "Electro-optic effect and birefringence in semiconductor vertical-cavity lasers," Phys. Rev. A **56**(1), 845–853 (1997).
29. T. Ackemann and M. Sondermann, "Characteristics of polarization switching from the low to the high frequency mode in vertical-cavity surface-emitting lasers," Appl. Phys. Lett. **78**(23), 3574–3576 (2001).
30. L. L. Chen, B. Q. Zhou, G. Q. Lei, W. F. Wu, Y. Y. Zhai, Z. Wang, and J. C. Fang, "Effects of temperature on Rb and 129Xe spin polarization in a nuclear magnetic resonance gyroscope with low pump power," AIP Adv. **7**(11), 115101 (2017).